# OTC 21294

# Gas hydrate occurrences and seafloor deformation: investigation of strain-softening of gas-hydrate bearing sediments and its consequence in terms of submarine slope instabilities.

N. Sultan and S. Garziglia, Ifremer and J.-L. Colliat, Total.



This paper was prepared for presentation at the Offshore Technology Conference held in Houston, Texas, USA, 2–5 May 2011.



## Abstract

Published laboratory geotechnical data by Masui and co-authors showed that increase in gas hydrates content tend to increase the peak shear strength and stimulate strain softening of the host sediment. Therefore, development of shear strains may lead to an important degradation of the shear strength (strain softening). In the present work, the strain softening of gas hydrate-bearing sediments was implemented in a 3D slope stability model (SAMU-3D). This was done by adding to the classical limit analysis method a shear strain field compatibility equivalent to the velocity field compatibility. Examples of slope failures related to strain softening behavior documented in the literature were used to test the model formulation.

The developed model was then used to assess the stability of a steep flank of a shale-cored anticline in the eastern part of the offshore Niger delta. Numerical modeling showed that the formation of gas hydrates in the shallow sedimentary layers could considerably affect the factor of safety of the studied slope. The present work showed clearly that the strain-softening behavior of gas hydrate-bearing sediments has relevance for the stability of submarine slopes.

## Introduction

Over the last 3 decades cases of submarine slope failures have been reported worldwide in areas where gas hydrate occurrence was proved or suspected. McIver (1981) was amongst the first authors to speculate about the possible link between gas hydrate and submarine slope failures. In the McIver's conceptual model, the excess pore pressure induced by hydrate dissociation and the decrease in sediment shear strength (loss of hydrate playing the role of cementing agent between sediment grains) are the two key factors increasing the susceptibility of a slope to failure. The causal factor of the hydrate dissociation in the McIver (1981) model is the continuous sedimentation, which induces the upward migration of the base of the Gas Hydrate Stability Zone (GHSZ). Afterwards, Kvenvolden (1994) has stated that an upward movement of the bottom of the GHSZ due to an increase of bottom water temperature may accelerate the process of slope failures associated to hydrate dissociation. Different authors have later developed several other hypotheses and theories supposing all that gas hydrate dissociation generated by pressure and/or temperature changes may lead to important excess pore pressure and lead to sediment deformations and slope instabilities (Kayen and Lee, 1991; Kvenvolden, 1999; Paull et al., 1996 and 2000). Although several authors have raised serious concerns regarding possible connections between gas hydrate melting and submarine slope failures, none conclusively demonstrate that (Grozic, 2010).

On the other hand, recent laboratory geotechnical data have clearly shown that the presence of gas hydrates may lead to higher peak strength of the host sediment and promote strain softening, that is, a post-peak decrease in strength with increasing strains (Masui et al., 2005, 2006, 2008). The experimental data presented by Masui et al. (2005) suggest that at large strains, the strength of gas hydrate-bearing sediments may reach a remolded value as low as that of their fully water saturated equivalents (i.e. similar void ratio without hydrates). To the authors' knowledge no published studies have yet investigated the potential impact of the strain softening behavior of gas hydrate-bearing sediments on submarine slope stability. The present work attempts to address theoretically this important question by implementing the strain-softening behavior of gas hydrate bearing-sediments in the SAMU-3D (Sultan et al. 2007a) software which is a three dimensional slope stability analysis model based on the limit analysis method. The developed software will then be used to assess the slope stability of the steepest flank of a shale-cored anticline forming a dome-shaped bathymetric high in the eastern part of the offshore Niger Delta.

## Strain softening behavior of marine sediments

### Background

Strain softening is a typical behavior of a range of natural soils such as microstructured clays, when bonds between particles are broken due to shearing, loose sands subjected to undrained loading as well as in dense sands during drained shearing (Leroueil and Hight, 2003; Gavali and Schweiger, 2010). By pointing out that the remolded strength of marine clays can be as low as 1/6 to 1/3 of their peak value, Kvalstad (2007) and Andresen and Jostad (2007) emphasized how strain softening is a central parameter in evaluation of the mechanism of progressive failure accounting for the development of large landslides in even gently dipping (< 2-3°) submarine slopes.

Laboratory studies have showed that gas hydrates can act as a bonding agent and thus have the effect of increasing sediments peak shear strength and sensitivity, St (i.e. the ratio of the peak to the remoulded strength). It is clearly observed on the laboratory tests conducted by Masui et al. (2005, 2006, 2008) on sandy sediments with degree of natural or synthetic methane hydrates saturation (volume fraction in pore space) higher than 20%. The results of the tests reported by Yun et al. (2007) on sand, silt and clay samples containing tetrahydrofuran hydrates (replacing methane hydrate) support the same conclusions and raise concerns about the relevance of strain softening behavior of hydrate-bearing sediments in slope stability evaluation.

### Proposition of a simple empirical expression

In order to include the strain softening behavior of a sensitive (i.e. strain softening) sediment in a slope stability analysis model, it is important to define a versatile curve allowing to describe the 3 main phases of a stress/strain curve going from the elastic behavior (shear strength development at relatively small shear strain) through the mobilization of the peak value ($\tau_p$) and finally the softening behavior (decrease of the shear strength from the peak strength to the remolded one) with progress of shear strain. In the present work, we propose the following expression giving the shear strength $\tau$ normalized with respect to the peak shear strength $\tau_p$ and as a function of shear strain $\gamma$:

$$\frac{\tau}{\tau_p} = \left[ \left(1 - \exp\left(-\beta.\gamma\right)\right) + \left(\exp\left(-\delta.\gamma^{\alpha}\right) - 1\right)\left(1 - \frac{1}{St}\right) \right] \quad (1)$$

Where $\beta$ corresponds to the elastic stiffness of the material and is proportional to the Young's modulus; St to the sensitivity and $\alpha$ and $\delta$ are two shape parameters used to describe the decrease of the shear strength from the peak value to the remolded one. Figure 1 shows the effect of the four control parameters on the shape of the stress/strain curve. Figures 1-a-b-c & -d describe, respectively, the increase of the elastic stiffness with $\beta$, the decrease of the remolded strength with the increase of St, the acceleration of the decrease of $\tau$ from the peak to the remolded value with the increase of $\alpha$ and the shrinkage of the peak plateau with the increase of $\delta$. Equation 1 allows determining for a given shear strain the mobilized shear strength $\tau$.

## 3-D slope stability modeling with strain softening behavior (SAMU-3D-SS)

The SAMU-3D software is a 3D slope stability analysis model developed by Sultan et al. (2007a) and is based on the limit analysis method and the upper bound theorem of plasticity (Michalowski, 1995, Chen et al., 2001a, b). The limit analysis is theoretically more rigorous than various simplified limit equilibrium methods that lead to significant errors as both kinematic and static admissibility are violated (Yu et al., 1998). SAMU-3D requires postulating 1) a valid failure surface that satisfies the mechanical boundary conditions and 2) a velocity field that satisfies the boundary conditions in the sediment delimited by the failure surface. In SAMU-3D, the postulated failure surface depends on 8 shape parameters and therefore is very flexible (Figure 2) in order to identify as accurately as possible the most critical failure surface. The intersection between the vertical plane of symmetry (Figure 2) and the seafloor is called the neutral line (NL). The 3D approach proposed in SAMU-3D approximates the failure surface by discretizing the sediment mass bounded by the postulated rupture surface into a number of prisms. For the velocity field, the sediment is considered as a Mohr–Coulomb material with an associative flow rule (Chen et al. 2001a). The postulated failure surface is considered as a limit state including material that is assumed to be plastic everywhere. The sediment will collapse if the work done by the external loads through any mechanism of collapse exceeds the internal plastic dissipation. Under these conditions, the upper bound theorem states that among all possible external loads applied to a kinematically admissible plastic zone, minimizing the work-energy balance equation (Rate of internal energy dissipation = Rate of external work) can approach the external load that brings failure. With the proposed method, the traditional definition of Factor of Safety (FOS) is conserved (FOS values greater than 1 means the slope is stable, while values lower than 1 means slope is instable) so that the results from the proposed model can be directly compared with other slope stability analysis methods. For a given load generated by external mechanisms, the 3D critical failure surface corresponding to the minimum FOS, is identified by means of an optimization with respect to the different shape parameters.

Indeed, the evaluation of the stability of a slope becomes a numerical problem of finding a set of variables that gives the minimum FOS.

**Evolution model: theoretical development**

In order to include the strain-softening behavior in SAMU-3D software, a shear strain field compatibility equivalent to the velocity field compatibility used in the limit analysis method is considered. Details concerning the velocity field compatibility can be found in Chen et al. (2001a). Zhang and Zhang (2007) have already used a similar development combining a compatible shear strain field to a 2D limit equilibrium method. The Zhang and Zhang (2007) model uses vertical slices which simplifies the determination of the shear strain field. In SAMU-3D software the orientation of the prisms is optimized in order to define the most critical failure surface.

For each shear strain $\gamma$ applied at the bottom of the first slice, the shear strain field is determined for the whole postulated failure volume. Using the stress/strain curve equivalent to the one presented in Figure 1, it is possible to calculate the mobilized shear strengths at the bottom of prisms and between adjacent prisms. For each shear strain $\gamma$ applied at the bottom of the first slice an FOS value is calculated (Figure 3). Zhang and Zhang (2007) consider that the true shear strain $\gamma$ should be the one that leads to the maximum FOS among all the possible values (Figure 3). However, by using the Zhang and Zhang (2007) method, the minimum shear strength mobilized between different adjacent prisms and at the bottom of each prism rarely reaches the remolded shear strength. We propose in the present work to consider the true shear strain $\gamma$ as the one leading to the reduction of the shear strength to its remolded value at least at one location along the NL (Figure 3). In the following the SAMU-3D software including the strain softening behavior is called SAMU-3D-SS.

## Illustrative examples

In the following, two examples reported in the literature (Hungr et al., 1989 and Andresen and Jostad, 2007) are reanalyzed using SAMU-3D-SS to investigate the validity of the proposed approach.

**Example from Hungr et al. (1989)**

The first example concerns a spherical failure surface in a purely cohesive soil characterized by a unit weight of 9.8 $kN/m^3$ and an undrained shear strength Su (or $\tau_p$) of 49.8 kPa. For the case where the sensitivity St is taken equal to 1, a FOS equal to 1.422 was obtained by Hungr et al. (1989) using the limit equilibrium method and a FOS of 1.422 obtained by Chen et al. (2001a) using the upper bound theorem. The minimum FOS calculated using SAMU-3D-SS is found equal to 1.43 as plotted in Figure 4. In order to study the effect of St on the FOS using SAMU3D-SS, 5 additional calculations with the same spherical failure surface were carried out by considering 5 different St values (=2, 4, 6, 10 and 15). Figure 4 shows that FOS decreases from 1.43 with St =1 to 0.802 for St=15. The decrease of the FOS with St is more pronounced between St=1 and 4 than between St=4 and St=15. A second set of calculations was done for a partially elliptic failure surface (M=2 which gives an ellipse in the x-y plane – see Figure 5-a). Figure 4 shows that the FOS decreases for this partially elliptic surface from 1.317 with St =1 to 0.724 for St=15 (Figure 4). The third set of calculations considers a more elliptic failure surface with an M value of 3 (Figure 5-b). The FOS decreases for this third calculation from 1.279 with St =1 to 0.695 for St=15 (Figure 4). For the fourth set of calculation, the parameter M was maintained constant (=3) but the 7 other parameters were optimized to find the most critical failure surface (see Figure 5-c for the shape of the failure surface). The mobilized shear strength at the base of the NL is also presented in Figure 5.

To the authors' knowledge no published studies have previously evaluated the 3D slope stability of strain softening, purely cohesive materials. That is why, and in order to compare the results obtained with SAMU-3D-SS with some reference calculations, we used FLAC/slope with the ubiquitous-joint model to evaluate the effect of the sensitivity on the FOS. The ubiquitous-joint model is an anisotropic plasticity model that includes weak planes of specific orientation embedded in a Mohr-Coulomb solid and where a peak and remolded strength can be defined. In large-strain mode, the orientation of the weak plane is adjusted to account for rigid body rotations, and rotations due to deformations (FLAC/Slope user's guide). The initial orientation of the weak planes is defined by the user and for the present example, 4 different orientations (0°, 45°, 60° and 90° see Figure 4) were considered. Results from FLAC/Slope are presented in Figure 4. The minimum FOS values are obtained by FLAC/Slope for weak layer orientations of 60°.

Although a) the ubiquitous-joint model used in FLAC/Slope is not a real strain softening model and b) the FLAC/Slope is a 2D and not a 3D slope stability analysis model, the FOS/St curves obtained using FLAC/Slope show a similar trend to those obtained using SAMU-3D-SS. This good agreement is probably related to the approach used in SAMU-3D which approximates the failure surface by discretizing the sediment mass bounded by the postulated rupture surface into a number of prisms and allows energy dissipation only at the base of prisms and between prisms.

**Example from Andresen and Jostad (2007)**

The second example was presented by Andresen and Jostad (2007) to study the mechanism of progressive failure in a long slope. The problem geometry simulates a 300 m long slope dipping at 4.2° and consisting of a 20 m thick layer of marine sensitive clays (St=1.53) deposited on top of firmer non-sensitive clay (Andresen and Jostad, 2007, Figure 7-a). Andresen and Jostad (2007) used the Plaxis software with the advanced model NGI-ANISOFT in order to evaluate the effect

of the sensitivity on the shape of the failure surface and to evaluate the load bearing capacity of an inclined slope. Results in terms of shape of the failure surface are presented in Figure 7-a showing the contour shadings of displacements plotted on deformed meshes for a perfectly plastic clay and a strain softening clay. Figure 7-a shows two different failure mechanisms obtained for the perfectly-plastic clay and that of strain-softening clay (Andresen and Jostad, 2007).The normalized failure loads for the perfectly plastic clay and the strain-softening clay were found equal to 4.35 and 3.56, respectively (Figure 8).

The Andresen and Jostad (2007) example was reanalysed using the SAMU-3D-SS software. The most critical surfaces obtained for St=1 and St=1.53 are respectively presented in Figure 7-b ("S" failure) and Figure 7-c ("L" failure). The shape and size of the two failure surfaces predicted by SAMU-3D-SS are very comparable to those predicted by Andresen and Jostad (2007). Seven calculations for 7 different applied loadings were carried out in order to define the normalized failure load for the "S" failure surface with St=1 (Figure 8). Six other calculations were necessary to determine the normalized failure load for the "L" failure surface with St=1.53 (Figure 8). The SAMU-3D-SS predicted normalized failure loads for the St=1.53 clay and the St=1 clay equal to 5.6 and 4.17, respectively. For the perfectly-plastic clay, two other calculations using Plaxis and FLAC/Slope with a Mohr-Coulomb model were carried out and the normalized failure loads were found equal to 4.74 (Plaxis) and 5.09 (FLAC/Slope) (Figure 8). For the perfectly-plastic clay with St=1, the normalized failure loads predicted using the SAMU-3D-SS software are, respectively, 10%, 18% and 25% higher than the values predicted using FLAC/Slope, Plaxis and NGI-ANISOFT (from Andresen and Jostad, 2007). For the strain-softening clay, the normalized failure load predicted using the SAMU-3D-SS software is 17% higher than the value found by Andresen and Jostad (2007) using the NGI-ANISOFT advanced soil model.

The difference between the predicted normalized failure loads of the different models presented in Figure 8 seems acceptable given the important discrepancy between the used i) geometry (2D versus 3D calculations) ii) theoretical and numerical methods (limit analysis versus Finite Element) and iii) rheological model (stress-strain curves). However, a more accurate validation of the SAMU-3D-SS software can be done using the FLAC-3D software with strain-softening model.

## Strain-softening of gas hydrate-bearing sediments: parameters fitting

The key features of gas hydrate-bearing sediments mechanical behavior are described in details by Soga et al. (2006). The three features that are essential to the proposed stress/strain-softening curve (equation 1) concern the increase of i) the elastic stiffness (Young Modulus, shear modulus), ii) the peak shear strength and iii) the sensitivity of the gas-hydrate-bearing sediments with the hydrate saturation. Thereafter, in order to reproduce the above three observations, the Masui et al. (2005) data presented in Figure 9-a are used to calibrate the different parameters of equation 1. These data are derived from tests carried out on synthetic methane hydrates formed within Toyoura sand samples. Table 1 summarizes the parameters used to fit the analytical expression proposed in this study to the Masui et al. (2005) data. The values of normalized peak shear strength ($\tau_p/\tau_{p\text{-}sat}$) versus hydrate saturation derived from the Masui et al. (2005) data (Figure 9-b) are used to define an empirical expression of $\tau_p$ versus the gas-hydrate saturation $S_h$:

$$\frac{\tau_p}{\tau_{p-sat}} = (1 - 2.22)\exp\left(-0.0006 S_h^{\,2}\right) + 2.22 \qquad (2)$$

The sensitivity, St, is derived from the peak shear strength (equation 2) and from the remolded shear strength which is independent of $S_h$. The normalized values of $\beta/\beta_{sat}$ versus $S_h$ derived from the experimental data of Masui et al. (2005) are plotted in Figure 9-c and used to define an empirical expression according to the following equation:

$$\frac{\beta}{\beta_{sat}} = (1 - 1.85)\exp(-0.07 S_h) + 1.85 \qquad (3)$$

Equations 2 and 3 are used to calculate a set of parameters (Table 2) for 6 different degrees of gas-hydrate saturation (0, 5, 15, 25, 40 and 50%). These sets of data are thereafter used to simulate the effect of the gas hydrate saturation on the stain/stress curves of the gas-hydrate bearing sediments.

## Case study from the Niger delta

### Geological setting, seafloor and sub-seafloor features

Lying in between ~700 and ~800 mbsl, in the eastern part of the offshore Niger Delta, the study area shows a dome-shaped bathymetric high culminating at ~ 50 m above the surrounding seafloor (Figure 10). Slope angles reach values of ~7° on the eastern flank of this dome-shaped feature formed by a shale-cored anticline. Higher slope angles delineate secondary morphological features such as seafloor undulations, pockmarks depressions, faults and escarpments (Figure 10). In one of

the most prominent escarpments running in a SW-NE direction along the eastern flank of the bathymetric high, the slope angles range in between 12° to 15°. The slightly arcuate shape of this escarpment makes it reminiscent of a landslide headscarp. This interpretation is however ambiguous since down-dip of the escarpment, no evidence of failed material can be clearly discerned on the seafloor. Analyses of 3D seismic lines also do not allow identifying landslide deposits, but interestingly reveal that the escarpment is located close to the sector where a bottom simulating reflector (BSR) apparently intersects the seafloor (Figure 11). The fact that gas-hydrates samples were collected (see Sultan et al., in prep) within the area were the BSR has been mapped on 3D seismic data (see Figure 11), is taken as a working hypothesis that gas hydrates may extend over a large sector within the upper sedimentary layers forming the dome-shaped bathymetric high. Overall, it raises suspicions as to a potential link between the occurrence of gas-hydrates in sediments and the evidences of slope instability such as the SW-NE escarpment and the seafloor undulations down the eastern flank of the bathymetric high.

**Geotechnical characterization**

The geotechnical characterization of the sediments covering the dome-shaped bathymetric high in the study area is based on in situ and laboratory testing. Two cone penetrations tests with pore pressure measurements (CPTu) were performed; one at site CS08 down to 25.5 mbsf, the second at site GS06 down to 30 mbsf (results in Figure 12). A 16.5 m long core was also collected at site CS08, while a core of 9.6 m long was collected at site GS06. Measurements conducted on both cores CS08 and GS06 included water content determination, oedometer tests, direct simple shear tests (DSS) and anisotropically consolidated undrained triaxial compression tests (CAUc) performed at in situ stress levels (Figure 12). Additionally, laboratory vane shear tests, fall cone tests and unconfined undrained triaxial compression tests were performed on core CS08. Besides, core GS06 was subjected to Multi Sensor Core Logging to determine the gamma density and to fall cone tests (Figure 12). Following the method proposed by Demers and Leroueil (2002) oedometer tests allowed through correlations with corrected tip resistance profiles (qt) from CPTu readings to derive continuous profiles of Yield Strength Ratio [YSR] using an empirical cone factor $N\sigma t = 3.68$ (Figure 12).

Based on the method presented by Lunne et al. (1997), correlations between undrained shear strength measurements (Su) performed on core and qt profiles allowed to derive continuous Su (or $\tau_p$) profiles using an empirical cone factor $Nkt = 18$. Continuous profiles of sensitivity (St) correspond to the ratio of Su and sleeve friction (fs) profiles as suggested by Lunne et al. (1997). Analyses of geotechnical logs reveal that at site CS08 and GS06, sediments consist essentially of normally consolidated clays characterized by Su increasing quasi linearly with depth. Differences between sites are however observed with Su increasing more slowly at site GS06 than at site CS08. It manifests at 25 mbsf by a value of Su being ~17 kPa lower at site GS06 than at site CS08. Besides the St derived from CPTu appears lower at site CS08 (St: 1-2) than at site GS06 (St: 1-5). Values of St in the range 2-5 as obtained from measurements on core are considered as more reliable. The geotechnical data presented in Figure 12 are used to define the geotechnical design parameters for water saturated sediments (Table 2).

## Undrained slope stability analysis using SAMU-3D-SS

One of the possible sources of shear strains accumulation and deformations for the studied site is creeping: seafloor undulations at the toe of the studied flank (Figure 10) could be the sign of these creep seafloor displacements. Creep accumulates shear strains over time leading to strain softening of the sediments and may induce instability in clayey slopes at strengths less than the peak strength (Hunter and Khalili, 2000). When sediment is sheared, generated excess pore pressure may (drained conditions) or may not (undrained conditions) dissipate depending on the permeability of the sediment and the time available. Both primary creep (decreasing strain rate with time) and secondary creep (creep at a constant strain rate) are relatively long processes and one may expect deformations under drained conditions. However, tertiary creep (strain rate is continuously increasing leading to the creep rupture) could occur under undrained conditions and may mobilize undrained strength properties. In the present work, the following two working hypotheses are considered a) creeping may be at the origin of shear strain developments and accumulations leading to strain softening of the material and b) the tertiary creep (accelerating strain rate to creep rupture or failure – Hunter and Khalili, 2000) occurs under undrained conditions mobilizing undrained shear strengths.

**Water-saturated sediments**

To get a reference analysis, the FOS against sliding of the eastern flank of the studied structure subject to its own weight is first calculated. Two calculations with water-saturated sediments and two different sensitivities (St=1 and St=3) are first carried out. The 3D geotechnical structure of the studied site is subdivided into 4 layers parallel to the seafloor with a maximum depth below the seafloor equal to 70 m. The geotechnical parameters characterizing the upper 30 m of water-saturated sediments (Table 3) are defined based on the lower bound of the laboratory and in situ geotechnical data presented in Figure 12. Geotechnical data were extrapolated for sediments between 30 and 60 mbsf.

The critical failure surface is found by two successive optimization procedures: the first optimization consists in finding the most critical NL while the second optimization process resides in finding, for a given NL, the prisms' orientation and the shape of the potential failure surface (Sultan et al. 2007a). 5000 sets of shape parameters for the 25 NL considered are tested. For the water-saturated sediments and for St=1, the FOS is found equal to 1.854. For the second calculation with St=3, the FOS drops by around 44% to 1.209. The 3D geometry of the most critical failure surface found for St=3 is presented in Figure 13. The length of the predicted failure surface along the NL is around 690 m and its maximum width is around 1250 m

(Figure 13-a). The maximum depth of the failure surface is equal to 34 m and is mobilizing sediments of the upper 3 layers (Figure 13-b). Finally, the normalized mobilized strength along the NL is decreasing from 0.602 at the toe of the slope to the remolded strength =1/3 at the top edge (Figure 13-c). It is worth noting this important decrease from a FOS of 1.854 for St=1 (stable slope) to a FOS of 1.209 for St=3 (metastable slope). Figure 14-a shows, on a bathymetric map, the projection of the most critical failure surface for the water-saturated sediment with St=3. In Figure 14-a are also indicated some of the seafloor undulations structures (see also Figure 10-b) below the toe of the predicted failure surface which could be an expression of creep seafloor displacements.

Figure 14-b illustrates the resulting bathymetry and slope angle map after removing the sediment mass above the critical failure surface presented in Figure 13. Interestingly, the width of the predicted failure surface is comparable to the width of the SW-NE escarpement reminiscent of a landslide headscarp as indicated in Figure 14-b. In order to more deeply evaluate the possible link between the strain softening of gas-hydrate bearing sediments and the "assumed" landslide headscarp additional geotechnical, geological and geophysical data are needed.

**Gas-hydrate-saturated sediments**

Twenty additional calculations are carried out in order to evaluate the link between the strain softening behavior of gas-hydrate bearing sediments and the slope stability of the eastern flank of the dome-shaped bathymetric high. More precisely, the aim of these additional calculations is to evaluate the effect of the gas hydrate saturation and the depth at which the gas hydrates were formed on the FOS values. To this aim, four different depths of hydrate formation (5, 10, 15 and 20 mbsf) and 5 different degrees of gas hydrate saturation (5, 15, 25, 40 and 60%) are considered. For these calculations, shape parameters defining the critical failure surface as presented in Figure 13 are considered (no optimization procedure) and the geotechnical parameters presented in Table 2 and Table 3 are used. Results of those 20 calculations in terms of FOS and as a function of hydrate saturation and depths of hydrate formation are presented in Figure 15. The depth of hydrates formation seems to influence drastically the FOS values. For hydrates formed at 5 mbsf and for a degree of gas hydrate saturation of 5%, the FOS drops from 1.205 (for water saturated sediments with St=3) to 0.64. This FOS increases then slightly with the hydrate saturation to reach 0.7 for hydrate saturation of 60%. The increase of FOS with the hydrate saturation is due to the fact that the remolded strength is not mobilized everywhere in the failed volume (see Figure 6) and that the increase of the peak strength due to the presence of gas hydrates may relatively increase the FOS. The same tendency can be observed for the three other depths of hydrates formation: low FOS at 5% of hydrate saturation (FOS= 0.796 @ 10 mbsf, 0.96 @ 15 mbsf and 1.094 @ 20 mbsf) with respect to the water-saturated sediments and a slight increase of FOS with hydrate saturations. Figure 15 shows that when accounting for strain softening processes, around 60% of hydrate saturation formed at 20 mbsf is needed to reach an FOS value (=1.194) comparable to the FOS (=1.209) of the water-saturated sediments.

Figure 15 demonstrates clearly that the strain softening process may completely erase (if the hydrates is formed in the superficial sedimentary layers) the supposed benefic effect of gas hydrates on their host sediments strength. However, FOS values presented in Figure 15 should be considered as a lower bound. Indeed, continuous sedimentation and deepening of the gas hydrate occurrence zone is expected to be accompanied by some vertical compactions of the gas hydrate-bearing sediments structures (Sultan et al., 2007b) which undoubtedly cause an increase of the undrained shear strength and a decrease of the sediments' sensitivity and therefore an increase of FOS. Moreover, initial working hypotheses considering homogeneous lateral gas hydrate distribution at a given depth and that tertiary creeping occurs under undrained conditions and mobilizes undrained shear strengths are two other important uncertainty factors.

## Conclusions

The present works aimed to study the strain softening of gas hydrates bearing sediments and its consequence in terms of submarine slope instabilities. An empirical expression of stress/strain curve for gas hydrate-bearing sediments going from the elastic behavior through the mobilization of the peak strength and finally the softening behavior with progress of shear strain was proposed and implemented in the 3D slope stability software SAMU-3D. The use of this new developed model (SAMU-3D-SS) to assess the slope stability of the steepest flank of a shale-cored anticline in the eastern part of the offshore Niger Delta showed clearly that strain softening of gas hydrates-bearing sediments could be prejudicial for submarine slope stabilities and may completely erase the supposed benefic effect of gas hydrates on their host sediments strength. The FOS values were shown to depend strongly on the depth at which hydrates were formed and on the degree of hydrate saturation. For the considered slope, gas hydrates formed at 10 mbsf with a degree of saturation of 15% reduced the FOS of the water saturated slope by 40%.

This work is a first step in studying the potential link between hydrate bearing sediments' behavior and slope instabilities and is based on hypotheses including some uncertainties (mainly creeping leading to strain softening of the hydrated sediments and undrained tertiary creeping). Furthermore, and due to the high sensitivity of FOS on the degree of gas hydrate saturation, the application of such model to real case studies requires a good knowledge of the gas hydrate distribution.

## Reference


Andresen, L., Jostad, H.P. 2007. Numerical modelling of failure mechanisms in sensitive soft clay- application to offshore geohazards. In: Conference, O.T. (Ed.), Offshore Technology Conference. OTC, Houston, Texas, p. 18650.

Chen, Z., Wang, X., Haberfield, C., Yin, J., Wang, Y., 2001a. A three dimensional slope stability analysis method using the upper bound theorem, Part I: theory and methods. International Journal of Rock Mechanics and Mining Sciences. 38: 369–378.

Chen, Z., Wang, J., Yin, J., Wang, Y., Haberfield, C., 2001b. A three dimensional slope stability analysis method using the upper bound theorem, Part II: numerical approaches, applications and extensions. International Journal of Rock Mechanics and Mining Sciences. 38: 379–397.

Demers, D., Leroueil, S. 2002. Evaluation of preconsolidation pressure and the overconsolidation ratio from piezocone tests of clay deposits in Quebec. Canadian Geotechnical Journal. 39: 174-192.

Gavali, V., Schweiger, H.F. 2010. Nonlocal multilaminate model for strain softening analysis. International Journal of Geomechanics, ASCE. 10(1): 30-44.

Grozic, J.L.H. 2010. Interplay Between Gas Hydrates and Submarine Slope Failure. Mosher et al. (Eds) Submarine Mass Movements and Their Consequences, Advances in Natural and Technological Hazards Research (28), 11-30.

Hungr, O., Salgado, F.M., Byrne, P.M. 1989. Evaluation of a three dimensional method of slope stability analysis. Canadian Geotechnical Journal. 26:679–86.

Hunter, G., Khalili, N. 2000. A simple criterion for creep induced failure of over-consolidated clays. In: Proceedings of the GeoEngineering 2000 Conference, Melbourne.

Kayen, R.E., Lee, H.J. 1991. Pleistocene slope instability of gas hydrate-laden sediment on the Beaufort Sea margin. Marine Geotechnology. 10:125–141.

Kvalstad, T.J. 2007. What is the Current "Best Practice" in Offshore Geohazard Investigations? A State-of-the-Art Review. In: Conference, O.T. (Ed.), Offshore Technology Conference. OTC, Houston, Texas, p. 18545.

Kvenvolden, K.A. 1999. Potential effects of gas hydrate on human welfare. Proceedings of the National Academy of Sciences of the USA 96:3420–3426.

Kvenvolden, K.A. 1994. Natural gas hydrate occurence and issues. Annuals of the New York Academy of Sciences. 715:232-246.

Leroueil, S., Hight, D. W. 2003. Behaviour and properties of natural soils and soft rocks. In : Characterization and engineering properties of natural soils, T. S. Tan, K. K. Phoon, D. W. Hight, and S. Leroueil (Eds)., Vol. 1, Balkema, Exton, p. 29–254.

Lunne, T., Robertson, P.K., Powell, J.J.M., 1997. Cone Penetration Testing in geotechnical practice. Blackie Academic and Professional, London. 312 pp.

Masui, A, Miyazaki, K., Haneda, H., Ogata, Y, and Aoki, K. 2008. Mechanical properties of natural gas hydrate bearing sediments retrieved from Eastern Nankai trough. In: Conference, O.T. (Ed.), Offshore Technology Conference. OTC, Houston, Texas, p. 19277.

Masui, A., Haneda, H., Ogata, Y.,Aoki, K. 2006. Triaxial Compression test on submarine sediment containing methane hydrate in deep sea off the coast off Japan. In : Proceedings of the 41st Annual Conference, Japanese Geotechnical Society.

Masui, A., Haneda, H., Ogata, Y., Aoki, K. 2005. Effects of methane hydrate formation on shear strength of synthetic methane mydrate sediments. In: Proceedings of the 15th International Offshore and Polar Engineering Conference, Seoul, 364-369.

McIver, R.D. 1982. Role of naturally occurring gas hydrates in sediment transport. American Association of Petroleum Geologist Bulletin. 66:789–792.

Michalowski, R.L., 1995. Slope stability analysis: a kinematical approach. Géotechnique 45 (2), 283–293.

Paull, C.K., Ussler III W., Dillon, W.P. 2000. Potential role of gas hydrate decomposition in generation submarine slope failures. In: Max M (ed.). Natural Gas Hydrate in Marine and Permafrost Environments. Dordrecht: Kluwer Academic, pp. 149–156.

Paull, C.K., Buelow, W.J., Ussler III W., Borowski, W.S. 1996. Increased continental margin slumping frequency during sea-level lowstands above gas hydrate-bearing sediments. Geology. 24:143–146.

Soga, K., Lee, S. L., Ng, M. Y. A., Klar, A. 2006. Characterisation and engineering properties of methane hydrate soils. In: Characterisation and Engineering Properties of Natural Soils, T. S. Tan et al.,(Eds). Vol.4 pp. 2591–2642, A. A. Balkema, Lisse, Netherlands.

Sultan, N., Gaudin, M., Berné, S., Canals, M., Urgeles, R., Lafuerza, S. 2007a. Analysis of slope failures in submarine canyon heads: an example from the Gulf of Lions. Journal of Geophysical Research. 112(F1): F01009.

Sultan, N. 2007b. Comment on “Excess pore pressure resulting from methane hydrate dissociation in marine sediments: A theoretical approach” by Wenyue Xu and Leonid N. Germanovich. Journal of Geophysical Research (112), B02103.

Sultan, N., Riboulot, V., Lanfumey, V., Ker, S., Marsset, B., Géli, L., Tary, J.-B ., Klingelhoefer, F., Voisset, M., Colliat, J.L., Adamy, J., Grimau, S, in prep. Dynamics of fault-fluid-hydrate system around a shale-cored anticline in deepwater Nigeria.

Yu, H.S., Salgado, R., Sloan, S.W., Kim, J.M. 1998. Limit analysis versus limit equilibrium for slope stability. Journal of Geotechnical and Geoenvironmental Engineering. 124 (1): 1-11.

Yun, T. S., Santamarina, J. C., Ruppel, C. 2007. Mechanical properties of sand, silt, and clay containing tetrahydrofuran hydrate, Journal of Geophysal Research. 112, B04106.

Zhang, G., Zhang, J-M. 2007. Simplified method of stability evaluation for strain-softening slopes. Mechanics Reaseach Communication. 34: 444-450.

**Table 1. Parameters used to fit the analytical expression (equation 1) proposed in this study to the Masui et al. (2005) tests.**

| $S_h$ (%) | $\tau_p$ | $\tau_r$ | St | $\beta$ | $\delta$ | $\alpha$ | $\tau_p/\tau_{p\text{-}sat}$ | $\beta/\beta_{sat}$ |
|---|---|---|---|---|---|---|---|---|
| 55.1 | 8120 | 2880 | 2.819 | 1.452 | 0.002 | 2.449 | 2.126 | 1.815 |
| 40.1 | 5860 | 2880 | 2.035 | 1.440 | 0.002 | 2.449 | 1.534 | 1.800 |
| 25.7 | 4730 | 2880 | 1.642 | 1.350 | 0.002 | 2.449 | 1.238 | 1.688 |
| 0.0 | 3820 | 2880 | 1.326 | 0.800 | 0.002 | 2.449 | 1.000 | 1.000 |

**Table 2. Set of parameters used to simulate the effect of the gas hydrate on the stain/stress curves of the study site.**

| $S_h$ (%) | St | $\beta_{sat}$ | $\delta$ | $\alpha$ | $\tau_p/\tau_{p\text{-}sat}$ | $\beta/\beta_{sat}$ |
|---|---|---|---|---|---|---|
| 0 | 3.000 | 2.45 | 0.002 | 3.8 | 1.000 | 1.000 |
| 5 | 3.045 | 2.45 | 0.002 | 3.8 | 1.018 | 1.251 |
| 15 | 3.462 | 2.45 | 0.002 | 3.8 | 1.154 | 1.553 |
| 25 | 4.145 | 2.45 | 0.002 | 3.8 | 1.382 | 1.702 |
| 40 | 5.259 | 2.45 | 0.002 | 3.8 | 1.753 | 1.798 |
| 50 | 5.843 | 2.45 | 0.002 | 3.8 | 1.948 | 1.824 |

**Table 3. Basic geotechnical data used to carry out undrained slope stability analysis using SAMU-3D-SS.**

| Layer | d (m) | $\tau_p$ (kPa) | St | $\gamma'$ (kN/m$^3$) |
|---|---|---|---|---|
| 1 | 10 | 6 | 3 | 3.5 |
| 2 | 30 | 23 | 3 | 4.5 |
| 3 | 50 | 47 | 3 | 5.5 |
| 4 | 70 | 70 | 3 | 6.0 |

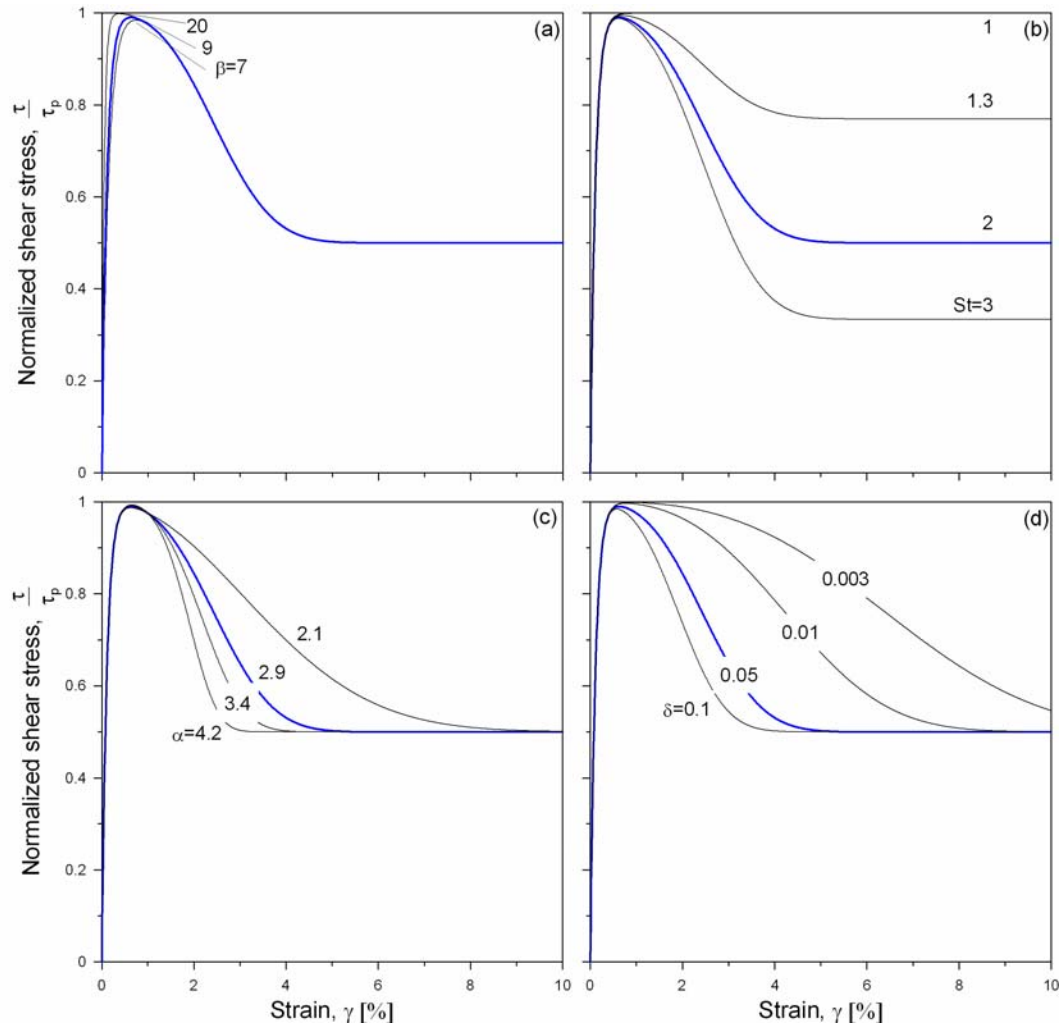


**Figure 1. Effect of four control parameters on the shape of the stress-strain curve a) β parameter, b) sensitivity St, c) α parameter and d) δ parameter.**

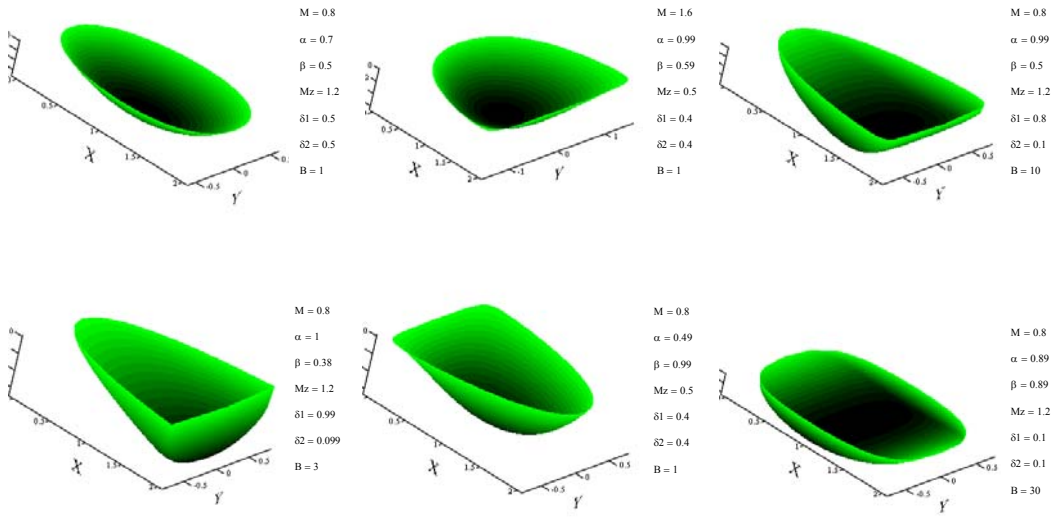


**Figure 2. Six failure surfaces generated by 6 different sets of parameters showing the flexibility of the shape of the failure surface used in SAMU-3D (from Sultan et al., 2007).**

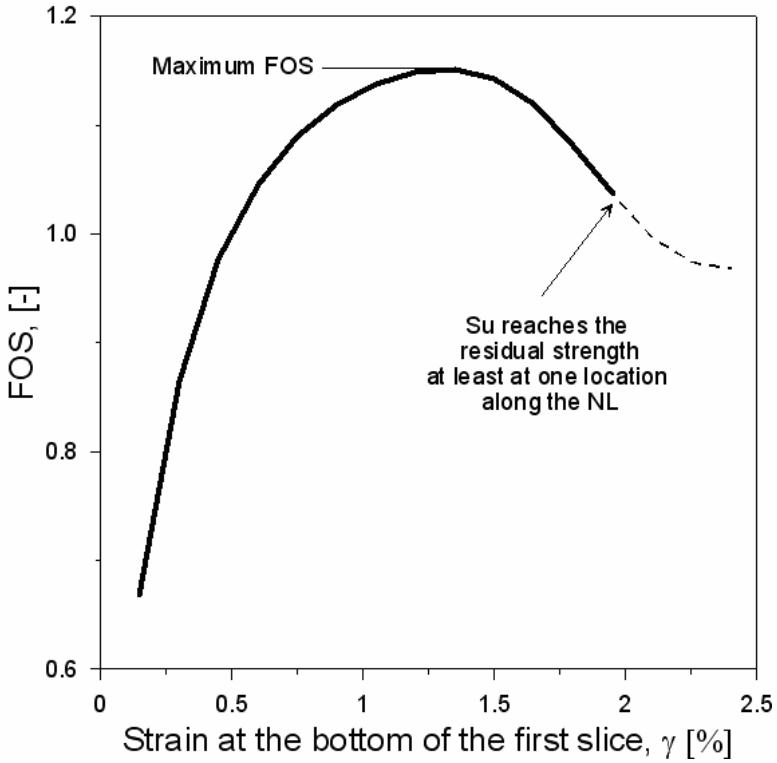


**Figure 3. Factor Of Safety versus shear strain at the bottom of the first slice. FOS is taken when the undrained shear strength reaches the residual strength at least at one location along the NL.**

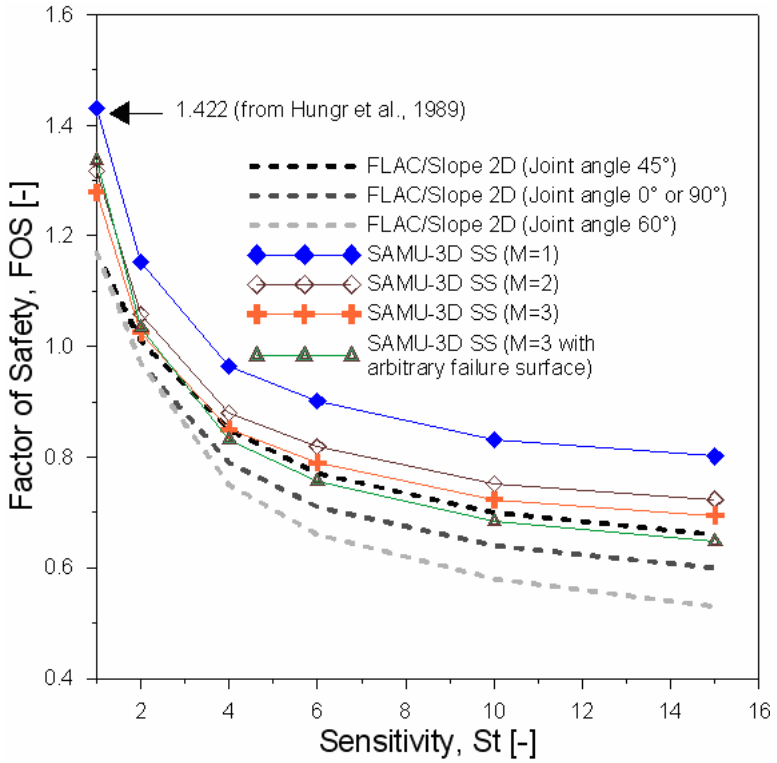


**Figure 4. Factor of Safety versus sediment sensitivities calculated for 4 different shapes of the failure surface. Results from FLAC/Slope using the "Ubiquitous" model for 4 different joint angle orientations are also plotted using dashed lines.**

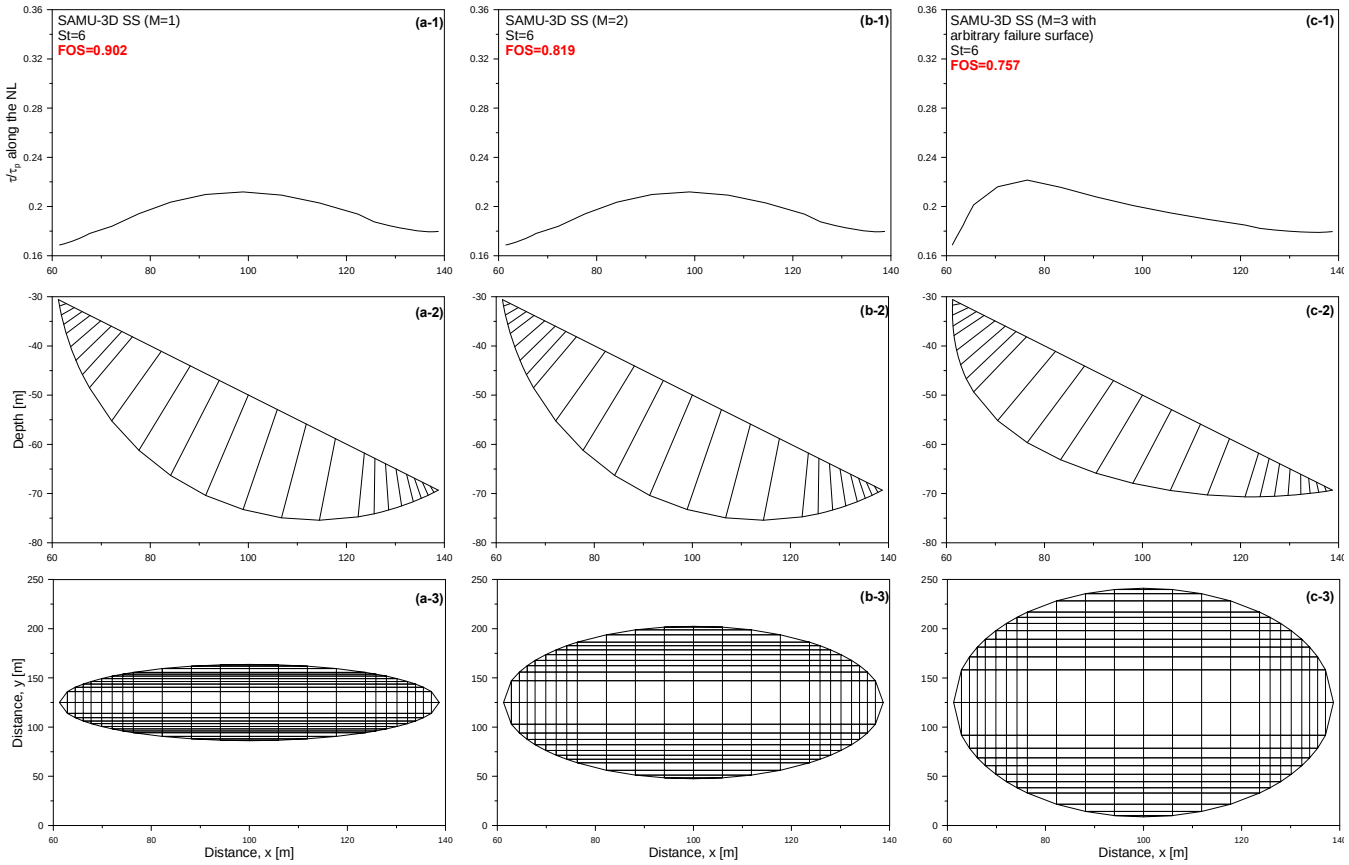


**Figure 5. Mobilized strength along the NL (-1), shape of the cross section along the NL (-2) and failure surface projected on the horizontal plane (-3) for St=6 and three different calculations a) M=1, b) M=2 and c) M=3 with arbitrary shape of the failure surface.**

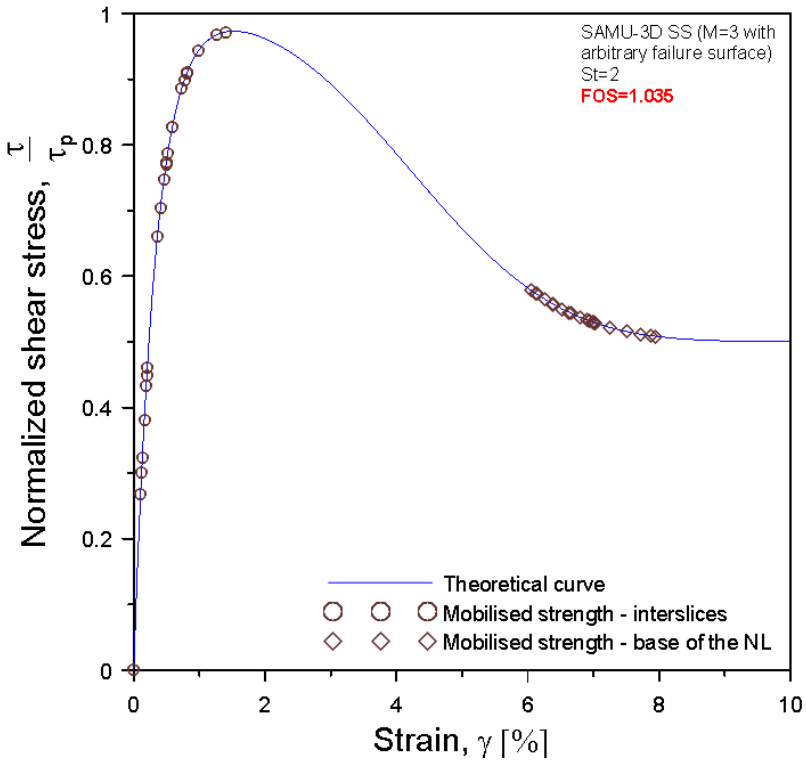


**Figure 6. Mobilized strength versus shear strain between interslices and along the NL for the calculation using M=3 and for an arbitrary shape of the failure surface.**

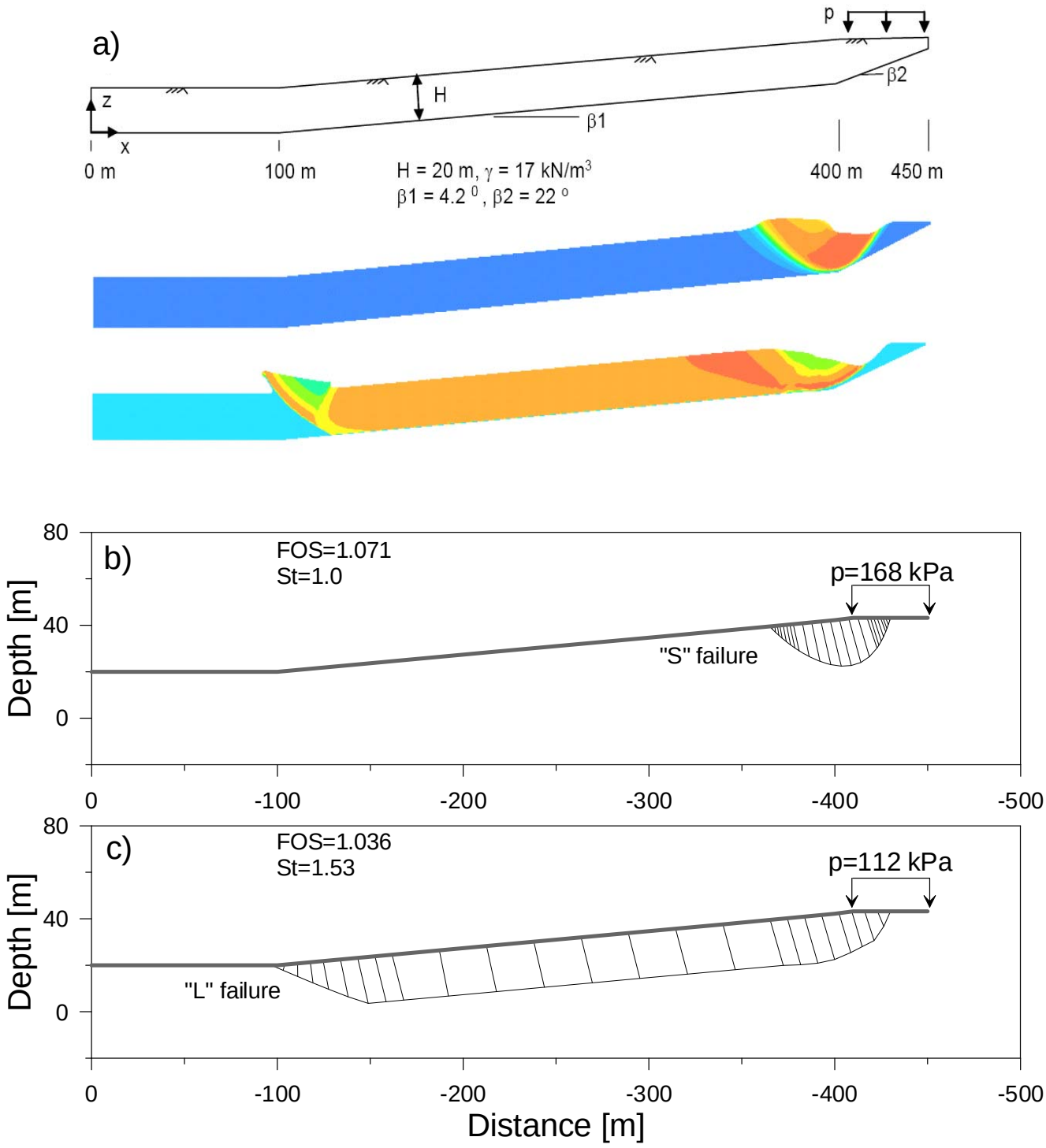


**Figure 7. a) Example from Andresen and Jostad (2007) showing the initial geometry and geotechnical parameters, contour shading of displacements plotted on deformed mesh for perfectly plastic clay and strain softening clay using the material model ANISOFT in Plaxis. b) Shape of the failure surface along the NL obtained with SAMU-3D for b) St=1 and c) St=1.53.**

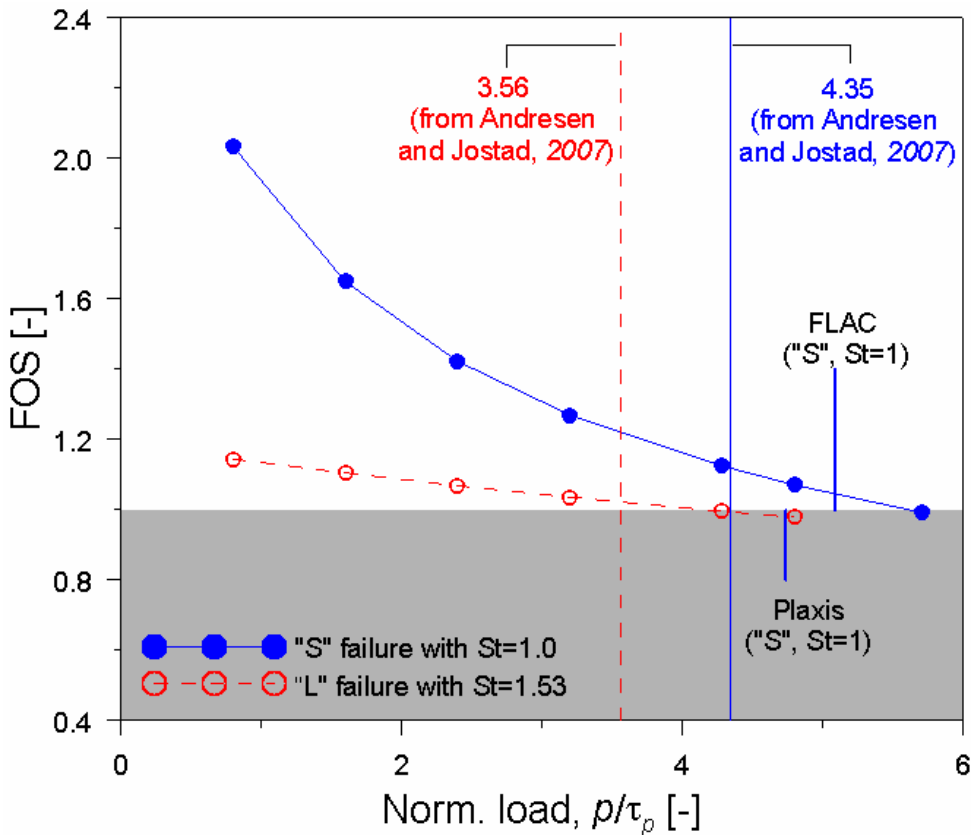


**Figure 8. FOS versus normalized loading $p/\tau_p$ obtained using SAMU-3D-SS for St=1 and St=1.53 and compared with the results obtained from Andresen and Jostad (2007) from FLAC/Slope and Plaxis.**

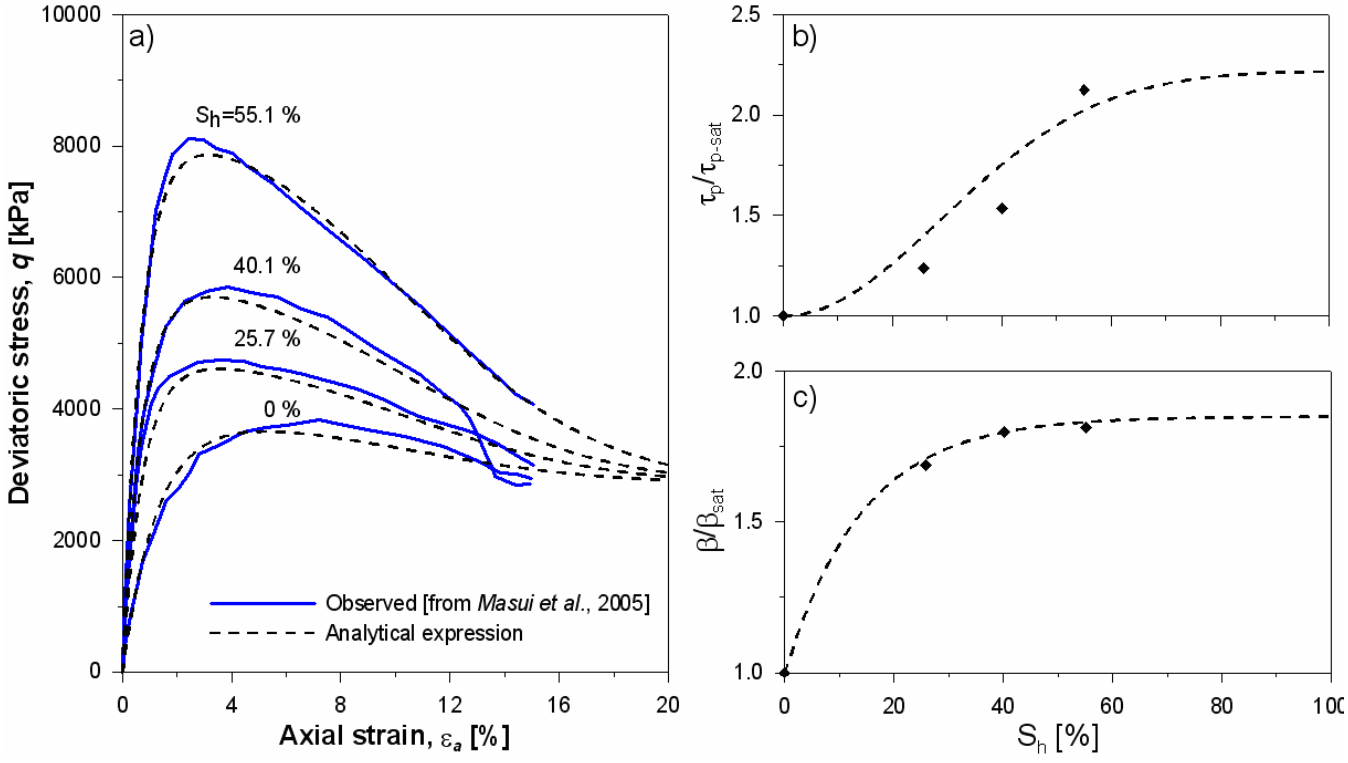


**Figure 9. a) Experimental data showing deviatoric stress/axial strain curves obtained by Masui et al. (2005) for gas-hydrate bearing sand samples compared to the analytical expressions proposed in the present work. Empirical expressions used in the present work to simulate the effect of the gas hydrate saturation on b) the peak deviatoric stress and c) the β parameter.**

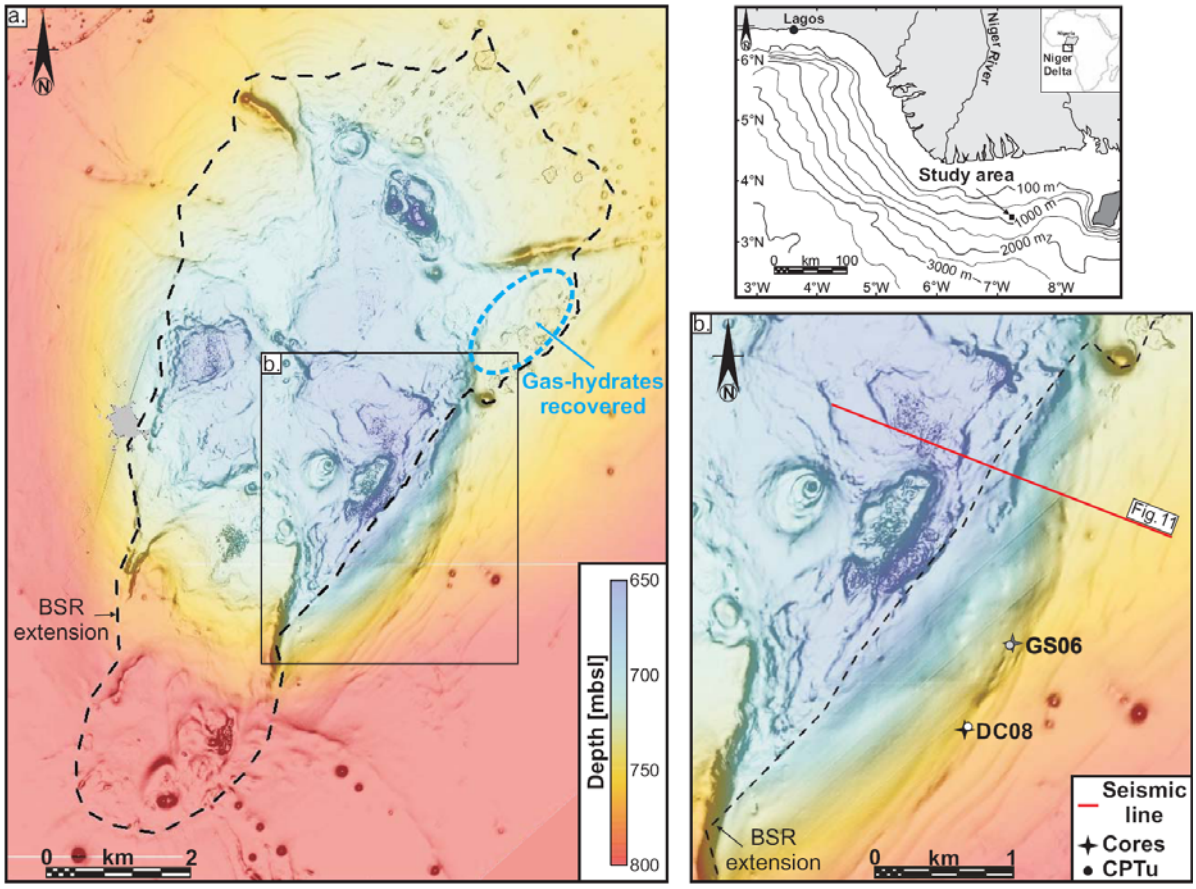


**Figure 10. a. Bathymetric map of the study area located in the eastern part of the deep-water Niger delta as indicated in the upper right inset. The bathymetric map is superimposed on a seafloor dip map enhancing morphological details in this dome-shaped area. The extension of a Bottom Simulating Reflector [BSR] as mapped on 3D seismic data (see Fig. 11) covering the whole area is indicated by the black dotted line. The light blue oval indicates the area where gas-hydrates were sampled as reported by Sultan et al. (in press). b. Location map showing, in close-up, the eastern flank of the dome-shaped bathymetric high typifying the study area.**

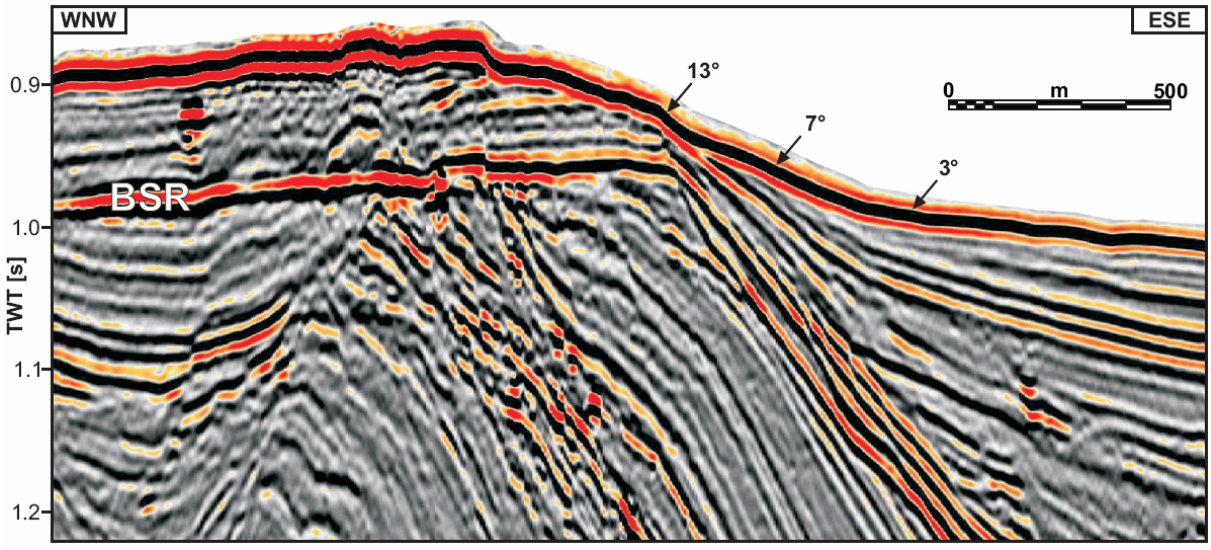


**Figure 11. 3D seismic line through the crest and eastern flank of the shale-cored anticline clearly showing a BSR at about 70 m below seafloor.**

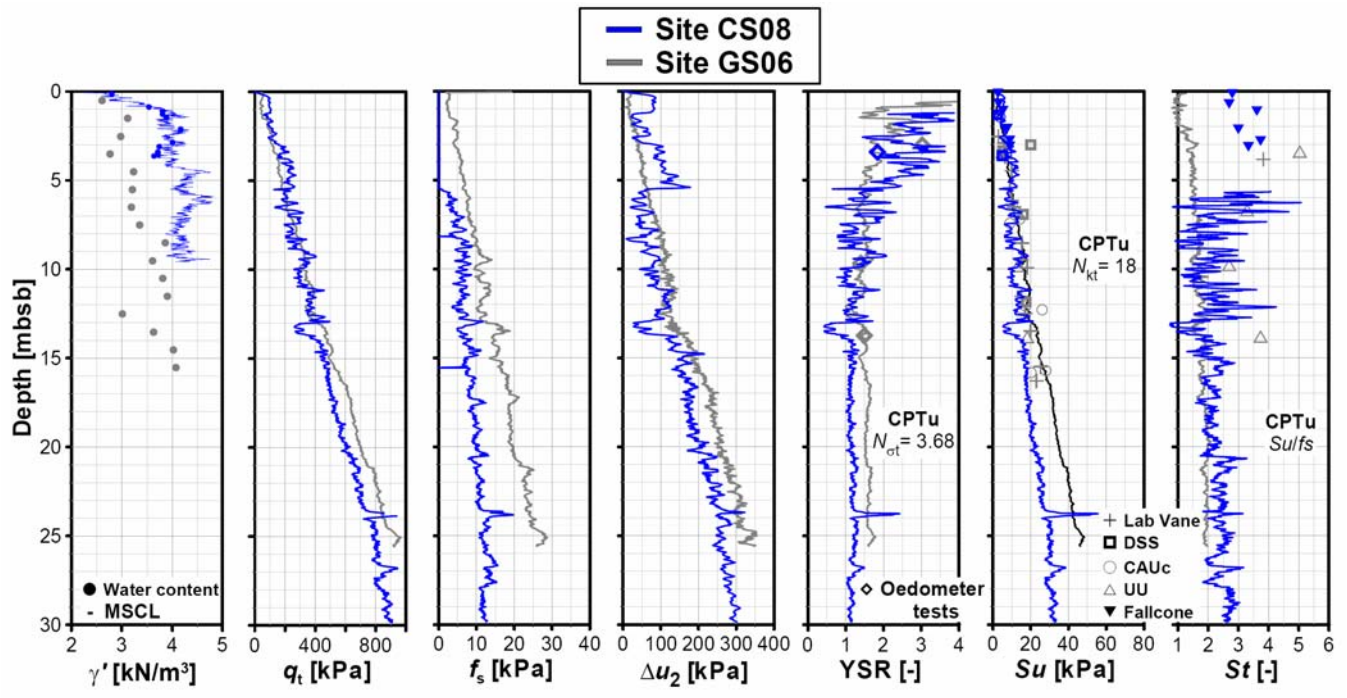


**Figure 12. Geotechnical logs of cores and CPTu at sites CS08 (in grey) and GS06 (in blue). Values of submerged unit weights γ' were obtained from water content measurements and automatic multi-sensor core logging. Correlations between measurements performed on cores, and CPTu data allowed to derive continuous profiles of Yield Strength Ratio [YSR], undrained shear strength [Su] and the sensitivity [St] as explained in the text.**

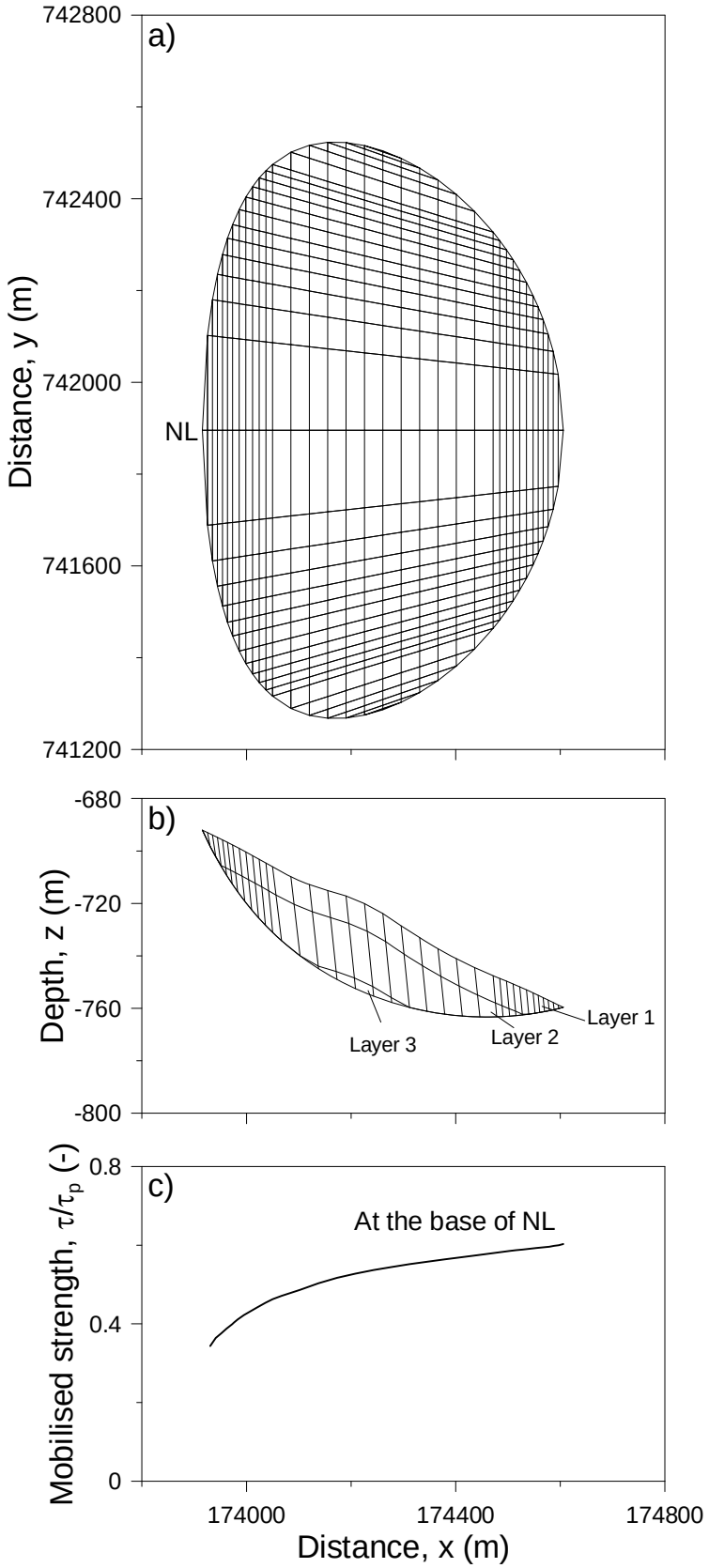


**Figure 13. Most critical failure surface for water-saturated sediment with St= 3 a) Failure surface projected on the horizontal plane, b) shape of the cross section along the NL and c) normalized mobilized strength along the NL.**

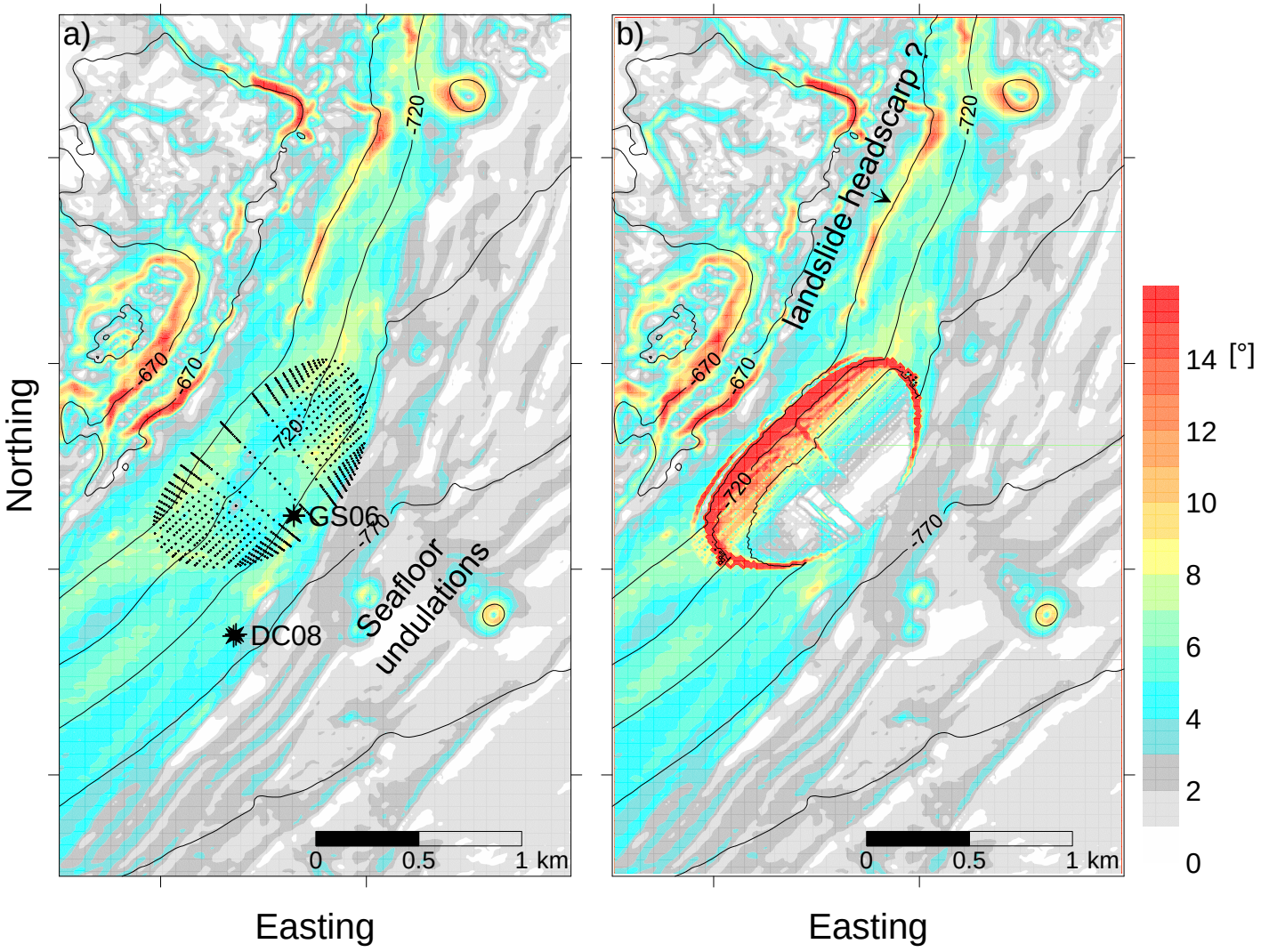


**Figure 14. a) The most critical failure surface (for water-saturated sediment with St= 3) obtained using SAMU-3D-SS projected on the initial bathymetry (contour interval 25 m) of the studied site and b) bathymetry and slope angle map modified by removing the sediment above the potential failure surface.**

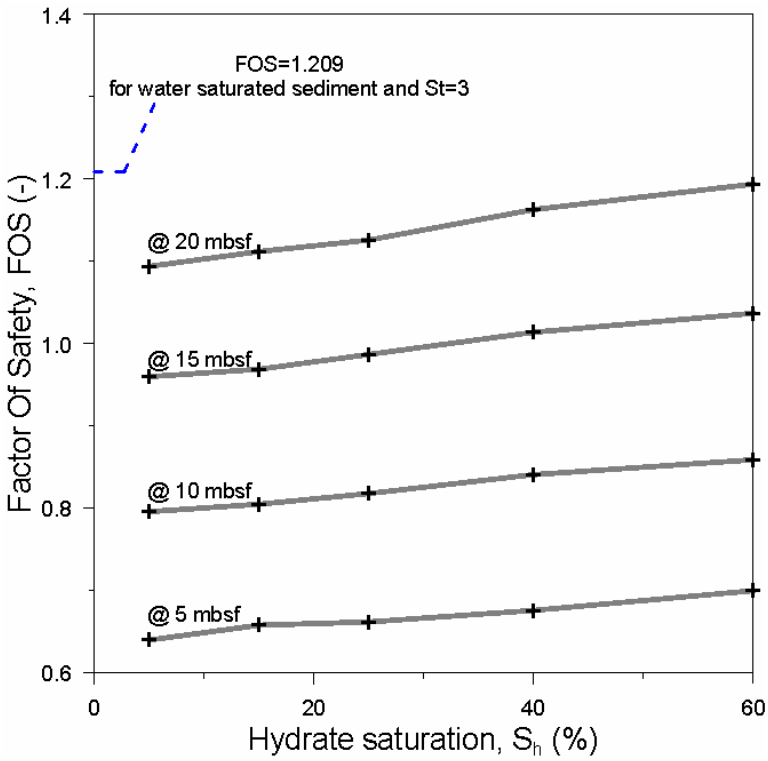


**Figure 15. FOS versus hydrate saturations (5 different degrees) and for 4 different case studies corresponding to the level at which the hydrate was formed. The FOS of 1.209 obtained for the water-saturated sediment and for St=3 is also indicated. An FOS of 1.854 was obtained for the case of water-saturated sediment with St=1.**